

Effect of Ce Substitution on the Magnetoresistivity and Flux Pinning Energy of the $\text{Bi}_2\text{Sr}_2\text{Ca}_{1-x}\text{Ce}_x\text{Cu}_2\text{O}_{8+\delta}$ Superconductors

B. Özçelik^a, C. Kaya^a, H. Gündoğmus^b, A. Sotelo^c, M. A. Madre^c

^aDepartment of Physics, Faculty of Sciences and Letters, Cukurova University, 01330 Adana, Turkey.

^bFaculty of Engineering, Hakkari University, 30000 Hakkari, Turkey.

^cICMA (CSIC-Universidad de Zaragoza), María de Luna, 3, 50018 Zaragoza, Spain.

Abstract

In this study, the effect of Ce doping on the properties of $\text{Bi}_2\text{Sr}_2\text{Ca}_{1-x}\text{Ce}_x\text{Cu}_2\text{O}_{8+\delta}$ ceramic superconductors, with $x = 0.0, 0.01, 0.05, 0.1,$ and 0.25 , has been investigated. Samples' precursors were prepared using the conventional solid state method and subsequently textured using the Laser Floating Zone technique. The magnetoresistance measurements were studied under various applied magnetic fields. The activation energies, irreversibility fields (H_{irr}), upper critical fields (H_{c2}) and coherence lengths at 0 K ($\xi(0)$) were calculated from the resistivity versus temperature ($\rho-T$) curves, under DC magnetic fields up to 5 T. The thermally activated flux flow model has been applied in order to calculate the flux pinning energies. The results indicated that $H_{c2}(0)$ varied from 416.19 to 115 T and the flux pinning energies varied from 1.46 to 0.042 eV at 0 T.

Keywords: Bi-based cuprates; XRD; Activation energy; LFZ-technique

Corresponding author: B. Özçelik. Department of Physics, Faculty of Sciences and Letters, Cukurova University, 01330 Adana, Turkey. E-mail: ozcelik@cu.edu.tr.

1. Introduction

Since the discovery of high- T_c superconductivity in the BSCCO system [1], intense studies have been performed on high- T_c BSCCO system in order to improve its critical temperature (T_c), critical current density (J_c), and better understand the structural, physical and magnetic properties of the superconducting phase [2–14]. These works have shown that the addition and/or substitution of rare-earth elements in the Ca/Cu site plays a critical role, not only leading to important changes in charge carrier concentration but also releasing the restriction of spin alignment due to the spin lattice interactions [15]. The effect of such changes is one of the important features that help to understand the structural details and superconducting properties along with the mechanism of occurrence of superconductivity [16–18]. On the other hand, the effect of substitution on the Cu sites is more important than in the Ca sites since the transition temperature in ceramic superconductors strongly depends on the charge carrier concentration in the Cu–O planes. It is well known that the holes in the Cu–O planes created by electron doping constitute an important parameter to achieve superconductivity.

In the typical ceramic high- T_c superconductors it is rather difficult to conceive the mixed state due to their short coherence length, large anisotropy and thermal energy. After the first prediction of flux creep by Anderson [19], many studies have been directed towards the effect of an applied external magnetic field on the resistive transition in order to understand the mechanism of flux pinning and flux motion [20–27]. There are several models for understanding the resistivity broadening under a magnetic field, such as thermally activated flux creep [22], flux flow [21], flux line melting and flux cutting [28]. The flux line can be thermally activated over the pinning energy barrier, even if the Lorentz force exerted on the flux bundle by the current is smaller than the pinning force. Some researchers have emphasized that a thermally activated flux creep model can describe the data quite well for the resistivity region near T_c ($\rho = 0$) [24,29–32].

It will be worthwhile to describe the material preparation technique which plays a crucial role, as important as the substitutions creating pinning centers in the BSCCO system. In addition, in order to produce very quickly a homogeneous sample, the polymer matrix route is one of best reported methods [33]. Other techniques used to improve the transport properties are based on the grain orientation which reduces the resistivity values by decreasing the number of weak links between grains [34,35].

Among all these techniques, the Laser Floating Zone Melting (LFZ) technique has been shown to be a very reliable process to obtain well-aligned Bi-2212 grains, with their c-axis nearly perpendicular to the growth direction, and very small amounts of secondary phases when they are properly annealed [7,8,36–39].

In previous works, the effect of Ce substitution for Ca on the physical and superconducting properties of Bi-2212 textured samples, using the LFZ method, has been studied [8]. The results have shown that Ce substitution is responsible for changes in both the magnetic and superconducting behavior in the superconducting state of the samples. In this work, the magnetoresistive properties of the Ce-substituted Bi-2212 textured samples will be studied. These properties will be interpreted using the thermally activated flux creep model on the magnetoresistance curves obtained under different magnetic fields between 0–5 T.

2. Experimental Details

Bi₂O₃ (98 %, Panreac), SrCO₃ (98+%, Panreac), CaCO₃ (98.5 %, Panreac), CuO (98 %, Panreac), and CeO₂ (99.9 %, Aldrich) commercial powders were weighed in the stoichiometric ratios of Bi₂Sr₂Ca_{1-x}Ce_xCu₂O_{8+δ} ($x = 0, 0.01, 0.05, 0.1, \text{ and } 0.25$). They were milled and calcined in air at 750 °C for 12 h. After the calcination process, the mixture was re-ground for 1 h and annealed under air at 800 °C for another 12 h. The prereacted homogeneous powders were then used to prepare 120 mm long and 3 mm in diameter cylindrical precursors, by cold isostatic pressing with an applied pressure of 200 MPa during 1 min. The obtained cylinders were subsequently used as feed in a directional solidification process performed in a laser floating zone (LFZ) melting installation described schematically in previous work [37]. The bars have been processed using a continuous power Nd:YAG laser ($\lambda = 1064 \text{ nm}$), under air, at a growth rate of 15 mm/h and a relative rotation of 18 rpm between seed and feed. After the texturing process, the samples were subjected to an annealing process consisting of two steps: 60 h at 860 °C, followed by 12 h at 800 °C and, finally, quenched in air to room temperature in order to avoid oxygen excess which could negatively affect the T_c values. X-ray diffraction patterns of the samples were recorded at room temperature using a Rigaku RadB powder diffractometer system working with CuK α radiation and a constant scan rate between $2\theta = 3\text{--}60^\circ$ at room temperature. Magnetoresistance measurements were performed by the conventional four-point probe technique under various applied magnetic fields of 0, 0.5, 1, 2, and 5 T. The external DC magnetic fields

for resistivity measurements were provided by an electromagnet and they were applied parallel to the current direction. Zero field cooling (ZFC) procedure was used during all measurements. The samples with $x = 0.0, 0.01, 0.05, 0.1,$ and 0.25 will be hereafter named as A, B, C, D and E, respectively.

3. Results and Discussion

Powder XRD patterns for all samples are presented in Fig. 1. In this figure it can be observed that all samples possess very similar diffraction patterns and major peaks correspond to the superconducting Bi-2212 phase (identified by + in Fig. 1e) independently of Ce content. The main differences are due to variations in the relative intensity of some peaks but it is due to an induced orientation of the plate-like grains during sample preparation for XRD experiments. Moreover, only very small amounts of CaCuO_2 nonsuperconducting secondary phase (indicated by * in Fig. 1) can be detected in the samples. This is a typical result in this kind of materials which show the main phase (Bi-2212) always accompanied by other unreacted nonsuperconducting secondary phases. In addition, no Ce-containing secondary phase is observed, indicating that all Ce atoms are incorporated into the crystal structure of Bi-2212 superconductor [40–42]. On the other hand, since (111) and (002) peaks of simple CeO_2 are very close to the Bi-2212 peaks at 28 and 33 degrees, the change of relative intensity of the peaks may result from the overlapping of Bi-2212 phase peaks and peaks from some Ce-rich phase. From these graphs it can be observed that the Bi-2212 phase crystal symmetry is tetragonal in all cases. Furthermore, from these data the lattice parameters have been calculated using the least squares method and it has been found that while a – b parameters fluctuate around 3.8231, c -parameter slightly decreases from 30.9518 to 30.8893 with increasing Ce contents. It can be due to the fact that the variation of the oxygen content on the lattice structure by substituting Ce^{3+} for Ca^{2+} ions can cause a reduction in the c -parameter.

In order to investigate the effect of Ce doping on the superconducting properties of the samples, resistivity measurements at different applied magnetic fields (0, 0.5, 1, 2, and 5 T) were performed and the obtained results are represented in Fig. 2. It can be seen that all the samples exhibit a metallic-like behavior above the critical temperature, indicating that Bi-2212 is the major phase and in agreement with the XRD data discussed previously. T_c is below ≈ 98 K which confirms that the high- T_c phase (Bi-2212) is the dominant one in the samples. By using the magnetoresistance curves given in Fig. 2, the

onset temperature (T_c^{onset}) related to the transition of isolated grains to the superconducting state, and offset temperature (T_c^{offset}) related to volume fraction of Bi-2212 phase and/or features of intergranular component [24,43–45] were evaluated and displayed in Table 1. The T_c^{onset} values are obtained from the crossing point of the linear fit of the highest slope and the metallic high temperature part of the $\rho(T)$ curve for each sample. As can be seen in Table 1, T_c^{onset} decrease from 110 K to 109 K for sample A, from 98.8 K to 98 K for sample B, from 98 K to 96.8 K for sample C, from 97 K to 95 K for sample D, and from 91.8 K to 75 K for sample E, for 0 and 5 T applied fields, respectively. This decrement results from decrease in the number of charge carriers in the sample. In other words, when the Ce atoms are doped into samples the number of charge carriers decreases. Hence, the superconducting properties are suppressed and T_c of samples diminishes as the Ce content increases. In addition, these shifts in the onset critical temperatures are due to the results of the fact being very close to transition temperature, and very small change between the normal and the superconducting resistivity. It is argued that only a small fraction of the carriers are superconducting [29]. Also, this behavior could be attributed to the strong intragrain pinning energy, which does not allow any vortex motion in the vicinity of critical temperature [30].

On the other hand, as the temperature is lowered, the resistivity becomes more sensitive to the applied magnetic field producing the broadening found in the tails of the resistivity curves. This implies that at lower temperatures there is a higher concentration of superconducting carriers. As a consequence, the difference between the resistivity measured at zero and under applied field becomes bigger [46], and weak Josephson type links associated with the grain-boundaries network or intergranular effects appear [47]. In summary, the zero resistivity temperature is strongly affected by the applied magnetic field, indicating a shift to considerably lower temperature as the applied magnetic field increases. This decrease on the critical transition temperatures with increasing Ce-content and applied magnetic field can be associated with not only the decrement in pinning ability but also on the raise of weak links between the superconducting grains and the motion of fluxons [48]. As it is well-known in high- T_c superconductors, the defects such as dislocations, twin planes, grain boundaries, and those produced by artificial methods, as the radiation-induced columnar defects, increase the concentration of efficient pinning centers [2,21,49,50]. On the other hand,

in type-II superconductors, when the driving Lorentz force per unit volume exceeds the pinning force per unit volume, electrical resistance appears and hence energy dissipation occurs. Since lowering the temperature increases the pinning force, a higher magnetic field is necessary to move the flux line from the pinning center [21].

Another important parameter of high- T_c superconductors is the irreversibility line (IL) which implies the change from the flux pinning dominating regime to the thermally activated flux flow (TAFF) one, where electrical resistance appears. The irreversibility field, $H_{irr}(T)$, of a superconductor is the magnetic field above which magnetization becomes reversible at a given temperature T . It can be deduced from the broadening of the resistivity under different applied magnetic fields for different temperatures [32]. In Fig. 3, the irreversibility magnetic field values have been plotted versus the offset temperatures determined from the values at $R = 0.1R(T_c^{onset})$ for samples A, B, C, D, and E. The irreversibility field limits H_{irr} of the samples under several applied fields in an H - T diagram generates an IL that separates the H - T plane into two regions labeled as the low temperature region and the high temperature one. In the low temperature region, the flux dynamics is dissipative and thus irreversible. On the other hand, in the high temperature region, the flux motion is free and magnetically reversible. As seen in Fig. 3 with increasing Ce-content H_{irr} decreases and IL shifts to lower temperatures. These results indicate that the strength of the pinning abilities is getting weaker with increasing Ce-content.

By using the $\rho = \rho_N (90\%)$ relation, where ρ_N is the normal state resistivity at the critical temperature, T_c^{onset} , related to each field value [51], the upper critical fields of samples are obtained and presented in Fig. 4. $H_{c2}(0)$, the upper critical magnetic field at the temperature $T = 0$ K can be estimated by using the Werthamer-Helfand-Hohenberg (WHH) formula [52] given as:

$$H_{c2}(0) = -0.693T_c \left(\frac{dH_{c2}(T)}{dT} \right)_{T_0}$$

Using T_c values determined from the midpoint of the linear fit of the highest slope of the resistivity curves at zero field given in Fig. 2, $H_{c2}(0)$ values have been calculated and plotted in Fig. 5. It can be easily seen that the $H_{c2}(0)$ values decrease from 416.19 to 115 Tesla, with the increasing Ce-content. The coherence length, ξ , which is one of the characteristic parameters of the superconductors, is thus often calculated by using the equation given as:

$$H_{c2}(0) = \frac{\phi_0}{2\pi\xi^2}$$

where Φ_0 is the quantum of flux ($2.07 \times 10^{-15} \text{ Tm}^2$) [53]. The graph of coherence lengths calculated from the equation given above at the temperature $T = 0 \text{ K}$ has also been illustrated in Fig. 5. As can be seen from the graph, $\xi(0)$ varied from 8.9 to 16.8 Å when the Ce content was raised. Similar results have been reported for the coherence length $\xi(0)$ and $H_{c2}(0)$ values in Bi-based superconductors [19,25,54,55].

As it is well known, sufficiently strong pinning causes a small vortex motion and the superconductor behaves as a perfect conductor. However, in the case of strong currents, the thermally activated flux creep arises and the vortices can hop from one pinning site to another. In some cases, this phenomenon occurs at a measurable rate [21]. In the framework of the thermally activated flux creep model, the broadening in the tail part of the resistivity curves for the high- T_c oxides superconductor can be expressed as:

$$\rho[H, T] = \rho_0 \exp[-U(H)/k_B T]$$

where U is the flux pinning energy or activation energy for flux flow, depending on the temperature and magnetic field, ρ_0 is the pre-exponential factor, and k_B is the Boltzmann constant [19,56–59]. The flux pinning energy or activation energy (U) play a crucial role as a potential energy barrier in order to keep the magnetic flux in the pinning center, and can be directly deduced from the slope of the plot of $\log(\rho/\rho_0)$ versus $1/T$ as exhibited in Fig. 6. In this figure, the value of ρ_0 at the temperature of 100 K was used for the calculations. The calculated U values from the slope of the linear part of the low resistivity region of Arrhenius graphs (in the range of $-1.5 > \ln(\rho/\rho_0) > -3$) have been presented in Fig. 7, for all samples. As can be seen from the figure, the activation energy, U , is significantly reduced with the raise on the Ce-content and the applied magnetic field. It is a clear indication of the weak link destruction in the intergranular coupling, and the contraction of distance between the pinning centers indicating a decrease of the energy barriers in the material [43]. In other words, the results indicate that the field dependence of the flux pinning or activation energy may be consistent with the weak links between the superconducting grains and grain misorientations leading to the creeping of the vortices. These results are in agreement with the previously reported results [19,24,26].

It will also be very worthwhile to point out the main differences between the curves in Fig. 7 observed for fields around 0.5 Tesla. From the figure, it can be clearly seen that above 0.5 Tesla applied field value, the magnetic field starts to penetrate the sample

through the intergranular areas. This can be associated with the existence of different superconducting levels within the samples at the intergranular region: the superconducting grains, the weak links, and the superconducting clusters [19,60,61]. It is clear that when the magnetic field is gradually increased from 0 to 5 T, the rate of decrease of pinning energy, U , is moderated. Thus, it would be reasonable to argue that in the sample A, the fraction of grains interconnected by strong-links (clusters) is very large compared with those present in the sample E. This suggests that in the former one, the penetrable intergranular region by the external applied magnetic field is lower than the one in the latter.

4. Conclusions

In the present study, $\text{Bi}_2\text{Sr}_2\text{Ca}_{1-x}\text{Ce}_x\text{Cu}_2\text{O}_{8+\delta}$ ($x = 0.0, 0.01, 0.05, 0.1, \text{ and } 0.25$) samples were prepared by a conventional solid state method and successfully textured by using the LFZ method. Powder XRD diagrams showed that samples with nearly single Bi-2212 phase have been obtained, independently of the nominal Ce content. The activation energies, irreversibility fields (H_{irr}), upper critical fields (H_{c2}) and coherence lengths at 0 K ($\xi(0)$) were evaluated from the resistivity versus temperature (ρ - T) curves, under DC magnetic fields up to 5 T. The thermally activated flux flow model has been applied in order to calculate the flux pinning energies. The results indicated that $H_{c2}(0)$ varied from 416.19 to 115 T, and the flux pinning energies varied from 1.46 to 0.042 eV at 0 T. The reason of flux pinning energy decrease may arise from the diminishing of energy barriers with increasing Ce content. The coherence length at zero temperature, $\xi(0)$, varies from 8.9 to 16.8 Å for the pure and the highest Ce doped samples, respectively.

Acknowledgements

This work is supported by the Research Fund of Çukurova University, Adana, Turkey, under grant contracts No: FEF2011YL27 and FEF2013BAP11. A. Sotelo and M.A. Madre wish to thank the Gobierno de Aragón (Research Group T12), for financial support. M.A. Madre also acknowledges the MINECO-FEDER (Project MAT2011-22719) for funding. The authors thank to Prof. Dr. Cabir Terzioglu from Abant İzzet Baysal University for his help during the magnetoresistance measurements.

References

1. H. Maeda, Y. Tanaka, M. Fukutomi, T. Asano, *Jpn. J. Appl. Phys.* 27, L209 (1988)
2. B. Ozkurt, A. Ekicibil, M.A. Aksan, B. Ozçelik, M.E. Yakıncı, K. Kiymac, *J. Low Temp. Phys.* 149, 105 (2007)
3. D. Yazıcı, B. Ozçelik, M.E. Yakıncı, *J. Low Temp. Phys.* 163, 370 (2011)
4. A. Sotelo, M. Mora, M.A. Madre, J.C. Diez, L.A. Angurel, G.F. de la Fuente, *J. Eur. Ceram. Soc.* 25, 2947 (2005)
5. L. Jiang, Y. Sun, X. Wan, K. Wang, G. Xu, X. Chen, K. Ruan, J. Du, *Physica C* 300, 61 (1998)
6. B. Özkurt, M.A. Madre, A. Sotelo, M.E. Yakıncı, B. Özçelik, *J. Supercond. Nov. Magn.* 25, 799 (2012)
7. H. Gundogmus, B. Özçelik, B. Özkurt, A. Sotelo, M.A. Madre, *J. Supercond. Nov. Magn.* 26, 111 (2013)
8. C. Kaya, B. Özçelik, B. Özkurt, A. Sotelo, M.A. Madre, *J. Mater. Sci., Mater. Electron.* 24, 1580 (2013)
9. S. Bal, M. Dogruer, G. Yıldırım, A. Varilci, C. Terzioglu, Y. Zalaoglu, *J. Supercond. Nov. Magn.* 25, 847 (2012)
10. M.E. Yakıncı, *J. Phys. Condens. Matter* 9, 1105 (1997)
11. B. Chattopadhyay, B. Bandyopadhyay, A. Poddar, P. Mandal, A.N. Das, B. Ghosh, *Physica C* 331, 38 (2000)
12. G. Ilonca, V. Toma, T.R. Yang, A.V. Pop, P. Balint, M. Bodea, E. Macocian, *Physica C* 460–462, 369 (2007)
13. X.L. Wang, J. Horvat, G.D. Gu, K.K. Uprety, H.K. Liu, S.X. Dou, *Physica C* 337, 221 (2000)
14. T. Yamamoto, I. Kakeya, K. Kadowaki, *Physica C* 460–462, 799 (2007)
15. Y. Ando, A.N. Lavrov, S. Komiya, K. Segawa, X.F. Sun, *Phys. Rev. Lett.* 87, 017001 (2001)
16. J.M. Tarascon, P. Barboux, G.W. Hull, R. Ramesh, L.H. Greene, M. Gariod, M.S. Hedge, W.R. Mckinnon, *Phys. Rev. B* 38, 4316 (1989)
17. H. Eisaki, N. Kaneko, D. Feng, L. Fengi, A. Damascelli, P.K. Mang, Z.X. Shen, M. Greven, *Phys. Rev. B* 69, 064512 (2004)
18. K. Fujita, T. Noda, K.M. Kojima, H. Eisaki, S. Uchida, *Phys. Rev. Lett.* 95, 097006 (2005)
19. P.W. Anderson, *Phys. Rev. Lett.* 9, 309 (1962)

20. M. Erdem, O. Ozturk, E. Yucel, S.P. Altintas, A. Varilci, C. Terzioğlu, I. Belenli, *Physica B* 406, 705–709 (2011)
21. M. Tinkham, *Phys. Rev. Lett.* 61, 1658 (1988)
22. T.T. Palstra, B. Batlogg, R.B. Van Dover, L.F. Scheemeyer, J.V. Waszczak, *Appl. Phys. Lett.* 54, 763 (1989)
23. D.H. Kim, K.F. Gray, R.T. Kampwirth, D.M. McKay, *Phys. Rev. B* 42, 6249 (1990)
24. B. Özkurt, B. Özçelik, *J. Low Temp. Phys.* 156, 22 (2009)
25. D. Yazici, M. Erdem, B. Özçelik, *J. Supercond. Nov. Magn.* 25, 1811 (2012)
26. D. Yazici, M. Erdem, B. Özçelik, *J. Supercond. Nov. Magn.* 25, 725 (2012)
27. D. Sharma, R. Kumar, V.P.S. Awana, *Solid State Commun.* 152, 941–946 (2012)
28. M.R. Mohammadzadeh, M. Akvahan, *Physica C* 390, 134 (2003)
29. T.T.M. Palstra, B. Batlogg, L.F. Schneemeyer, J.V. Waszczak, *Phys. Rev. Lett.* 61, 1662 (1988)
30. A.P. Malozemoff, T.K. Worthington, E. Zeldov, N.C. Yeh, M.W. McElfresh, in *Strong Correlation and Superconductivity*, ed. by H. Fukuyama, S. Maekawa, A.P. Malozemoff, *Springer Series in Sol. State Sci.*, vol. 89 (Springer, Berlin, 1989)
31. R. Griessen, *Phys. Rev. Lett.* 64, 1674 (1990)
32. R.C. Ma et al., *Physica C* 405, 34 (2004)
33. A. Sotelo, H. Szillat, P. Majewski, F. Aldinger, *Supercond. Sci. Technol.* 10, 717 (1997)
34. S. Marinel, D. Bourgault, O. Belmont, A. Sotelo, G. Desgardin, *Physica C* 315, 205–214 (1999)
35. V. Garnier, R. Caillard, A. Sotelo, G. Desgardin, *Physica C* 319, 197–208 (1999)
36. A. Sotelo, M. Mora, M.A. Madre, J.C. Diez, L.A. Angurel, G.F. de la Fuente, *J. Eur. Ceram. Soc.* 25, 2947 (2005)
37. G.F. de la Fuente, A. Sotelo, Y. Huang, M.T. Ruiz, A. Badia, L.A. Angurel, F. Lera, R. Navarro, C. Rillo, R. Ibañez, D. Beltran, F. Sapiña, A. Beltran, *Physica C* 509, 185 (1991)
38. M.F. Carrasco, F.M. Costa, R.F. Silva, F. Gimeno, A. Sotelo, M. Mora, J.C. Diez, L.A. Angurel, *Physica C* 415, 163 (2004)
39. B. Özçelik, B. Özkurt, M.E. Yakıncı, A. Sotelo, M.A. Madre, *J. Supercond. Nov. Magn.* 26, 873 (2013)
40. S. Vinu, P.M. Sarun, A. Biju, R. Shabna, P. Guruswamy, U. Syamaprasad, *Supercond. Sci. Technol.* 21, 045001 (2008)

41. S. Vinu, P.M. Sarun, R. Shabna, A. Biju, U. Syamaprasad, *Mater. Lett.* 62, 4421 (2008)
42. R. Shabna, P.M. Sarun, S. Vinu, A. Biju, U. Syamaprasad, *Supercond. Sci. Technol.* 22, 045016 (2009)
43. D. Yazici, B. Ozcelik, *J. Supercond. Nov. Magn.* 25, 293 (2012)
44. G. Yildirim, S. Bal, A. Varilci, *J. Supercond. Nov. Magn.* 25, 1665 (2012)
45. R. Awad, A.I. Abou-Aly, M.M.H. Abdel Gawad, I G-Eldeen, *J. Supercond. Nov. Magn.* 25, 739 (2012)
46. N.G. Gomaa, *Egypt. J. Solids* 22, 256 (1999)
47. G.L. Bhalla Pratima, A. Malik, K.K. Singh, *Physica C* 391, 17 (2003)
48. A.M. Ianculescu, B. Despax Gartner, V. Bley, Th. Lebey, R. Gavrilă, M. Modreanu, *Appl. Surf. Sci.* 253, 344–348 (2006)
49. Y. Liu, X.G. Li, *J. Appl. Phys.* 99, 053903 (2006)
50. A. Jukna, I. Barboy, G. Jung, S.S. Banerjee, Y. Myasoedov, V. Plausinaitiene, A. Abrutis, X. Li, D. Wang, R. Sobolewski, *Appl. Phys. Lett.* 87, 192504 (2005)
51. M. Mudgel, L.S. Sharath Chandra, V. Ganesan, G.L. Bhalla, H. Kishan et al., *J. Appl. Phys.* 106, 033904 (2009)
52. N.R. Werthamer, E. Helfand, P.C. Hohenberg, *Phys. Rev.* 147, 295 (1966)
53. H.C. Yang, L.M. Wang, *Phys. Rev. B* 59(13) (1999)
54. J.G. Chigvinadze, A.A. Iashvili, T.V. Machaidze, *Phys. Lett. A* 300, 524 (2002)
55. H. Gundogmus, B. Özçelik, A. Sotelo, M.A. Madre. doi:10.1007/s10854-013-1135-0
56. P.W. Anderson, Y.B. Kim, *Rev. Mod. Phys.* 36, 39 (1964)
57. T.P. Sheahen, *Introduction to High-Temperature Superconductivity* (Kluwer Academic, Dordrecht, (2002)
58. T.T. Palstra, B. Batlogg, R.B. van Dover, L.F. Schneemeyer, J.V. Waszczak, *Phys. Rev. B* 41, 6621 (1990)
59. A.I. Abou-Aly, S.A. Mahmoud, R. Awad, M.M.E. Barakat, *J. Supercond. Nov. Magn.* 23, 1575 (2010)
60. E. Govea-Alcaide, I. Garcia-Fornaris, P. Mune, R.F. Jardim, *Eur. Phys. J. B* 58, 373 (2007)
61. P. Mune, E. Govea-Alcaide, R.F. Jardim, *Physica C* 384, 491 (2003)

Table 1. T_c^{onset} and T_c^{offset} values of the samples at various applied magnetic field

| Samples | 0 Tesla | 0.5 Tesla | 1 Tesla | 2 Tesla | 5 Tesla |
|-----------------|--|--|---|--|---|
| Sample A | $T_c^{onset}=110\text{K}$ $T_c^{offset}=95.9\text{K}$ | $T_c^{onset}=109\text{K}$ $T_c^{offset}=95.8\text{K}$ | $T_c^{onset}=109\text{K}$ $T_c^{offset}=95.4\text{K}$ | $T_c^{onset}=109\text{K}$ $T_c^{offset}=94.7\text{K}$ | $T_c^{onset}=109\text{K}$ $T_c^{offset}=91\text{K}$ |
| Sample B | $T_c^{onset}=98.8\text{K}$ $T_c^{offset}=92\text{K}$ | $T_c^{onset}=98.6\text{K}$ $T_c^{offset}=90\text{K}$ | $T_c^{onset}=98.3\text{K}$ $T_c^{offset}=89.5\text{K}$ | $T_c^{onset}=98.1\text{K}$ $T_c^{offset}=88\text{K}$ | $T_c^{onset}=98\text{K}$ $T_c^{offset}=87\text{K}$ |
| Sample C | $T_c^{onset}=98\text{K}$ $T_c^{offset}=93\text{K}$ | $T_c^{onset}=97.6\text{K}$ $T_c^{offset}=89\text{K}$ | $T_c^{onset}=97.3\text{K}$ $T_c^{offset}=87.8\text{K}$ | $T_c^{onset}=97\text{K}$ $T_c^{offset}=86\text{K}$ | $T_c^{onset}=96.8\text{K}$ $T_c^{offset}=83\text{K}$ |
| Sample D | $T_c^{onset}=97\text{K}$ $T_c^{offset}=90\text{K}$ | $T_c^{onset}=95.5\text{K}$ $T_c^{offset}=80\text{K}$ | $T_c^{onset}=95.3\text{K}$ $T_c^{offset}=77\text{K}$ | $T_c^{onset}=95\text{K}$ $T_c^{offset}=74\text{K}$ | $T_c^{onset}=95\text{K}$ $T_c^{offset}=66\text{K}$ |
| Sample E | $T_c^{onset}=91.8\text{K}$ $T_c^{offset}=58\text{K}$ | $T_c^{onset}=90.7\text{K}$ $T_c^{offset}=50\text{K}$ | $T_c^{onset}=88.2\text{K}$ $T_c^{offset}=46\text{K}$ | $T_c^{onset}=88\text{K}$ $T_c^{offset}=42\text{K}$ | $T_c^{onset}=75\text{K}$ $T_c^{offset}=36\text{K}$ |

Figure captions

Figure 1. X-Ray diffraction patterns of the samples A, B, C, D and E

Figure 2. Temperature dependence of resistivity for various applied magnetic field for the samples A, B, C, D and E

Figure 3. Temperature dependence of the irreversibility field of the samples A, B, C, D and E

Figure 4. Temperature dependence of upper critical magnetic field $H_{c2}(T)$ for the samples A, B, C, D and E

Figure 5. Variation of the upper critical magnetic field at the temperature $T = 0$ K, $H_{c2}(0)$, and coherence length, ξ , values versus Ce content

Figure 6. The Arrhenius plot of the resistivity of samples A, B, C, D and E

Figure 7. The flux pinning energy U versus applied magnetic field for the samples A, B, C, D and E

Figure 1

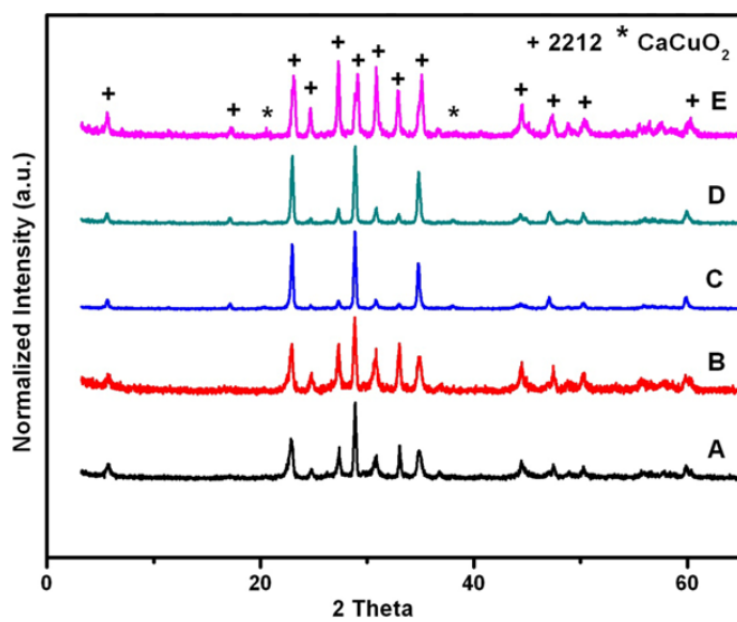


Figure 2

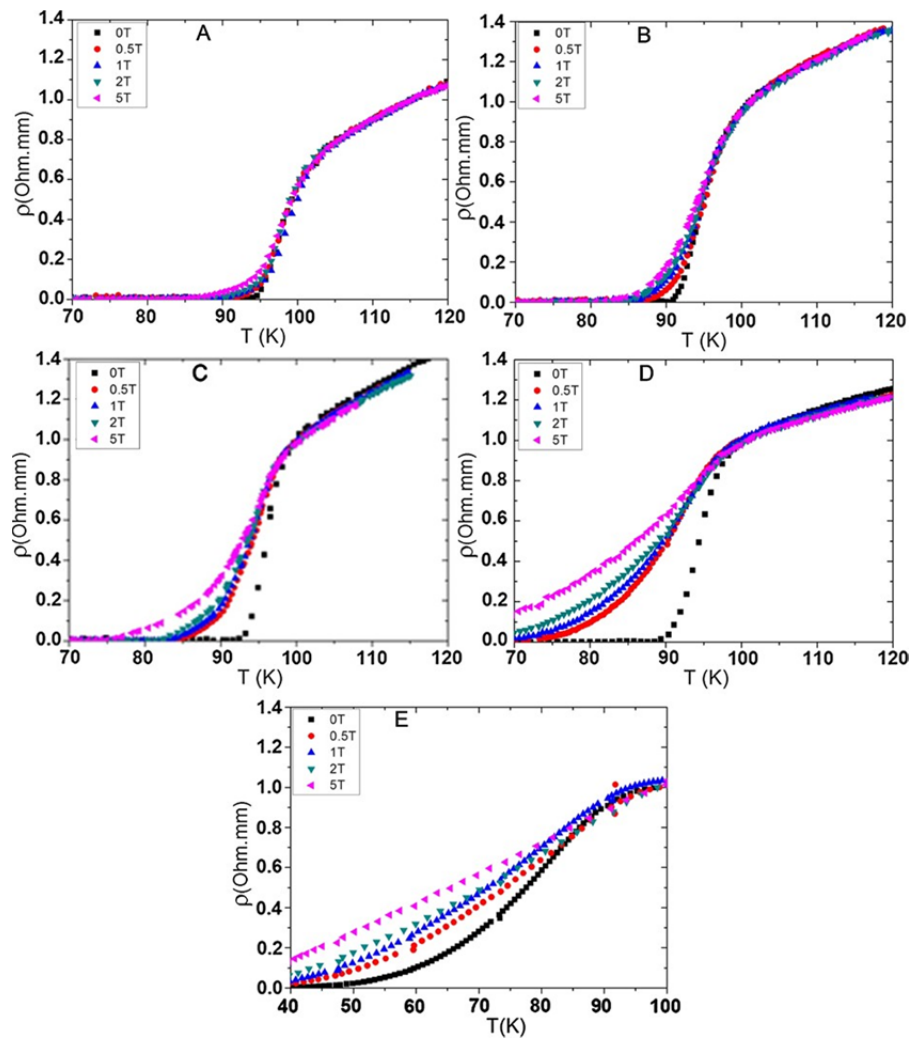


Figure 3

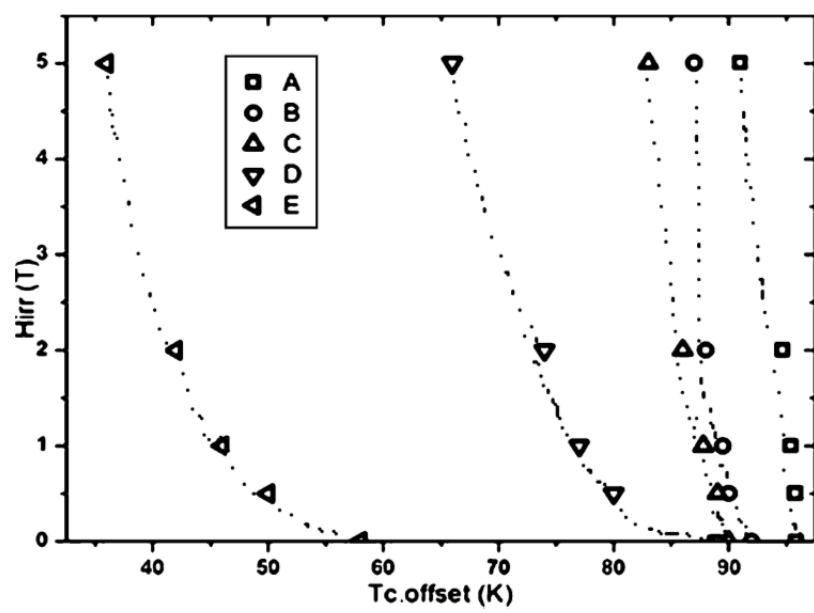


Figure 4

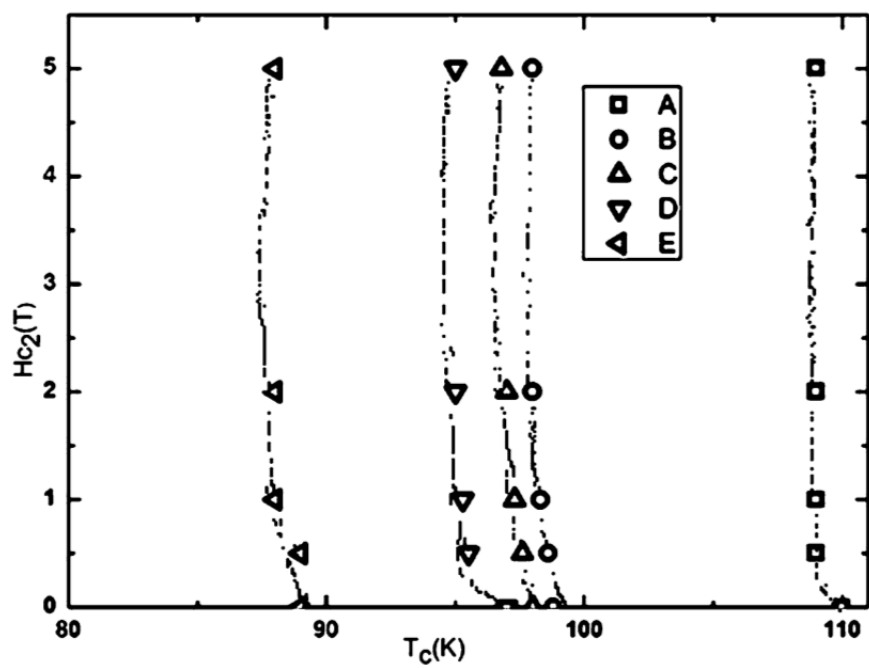


Figure 5

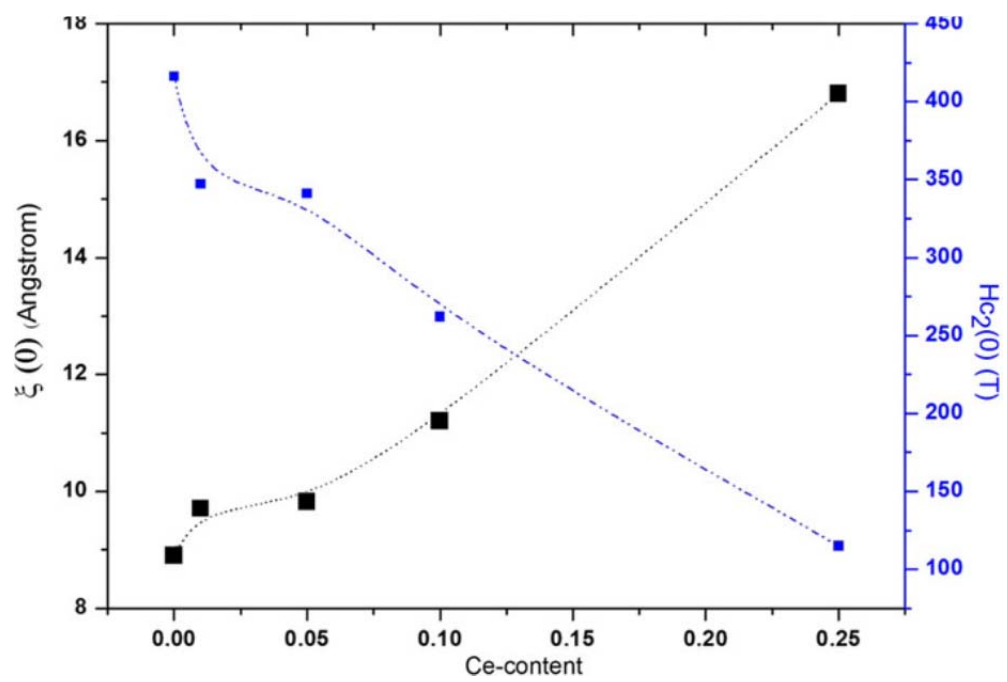


Figure 6

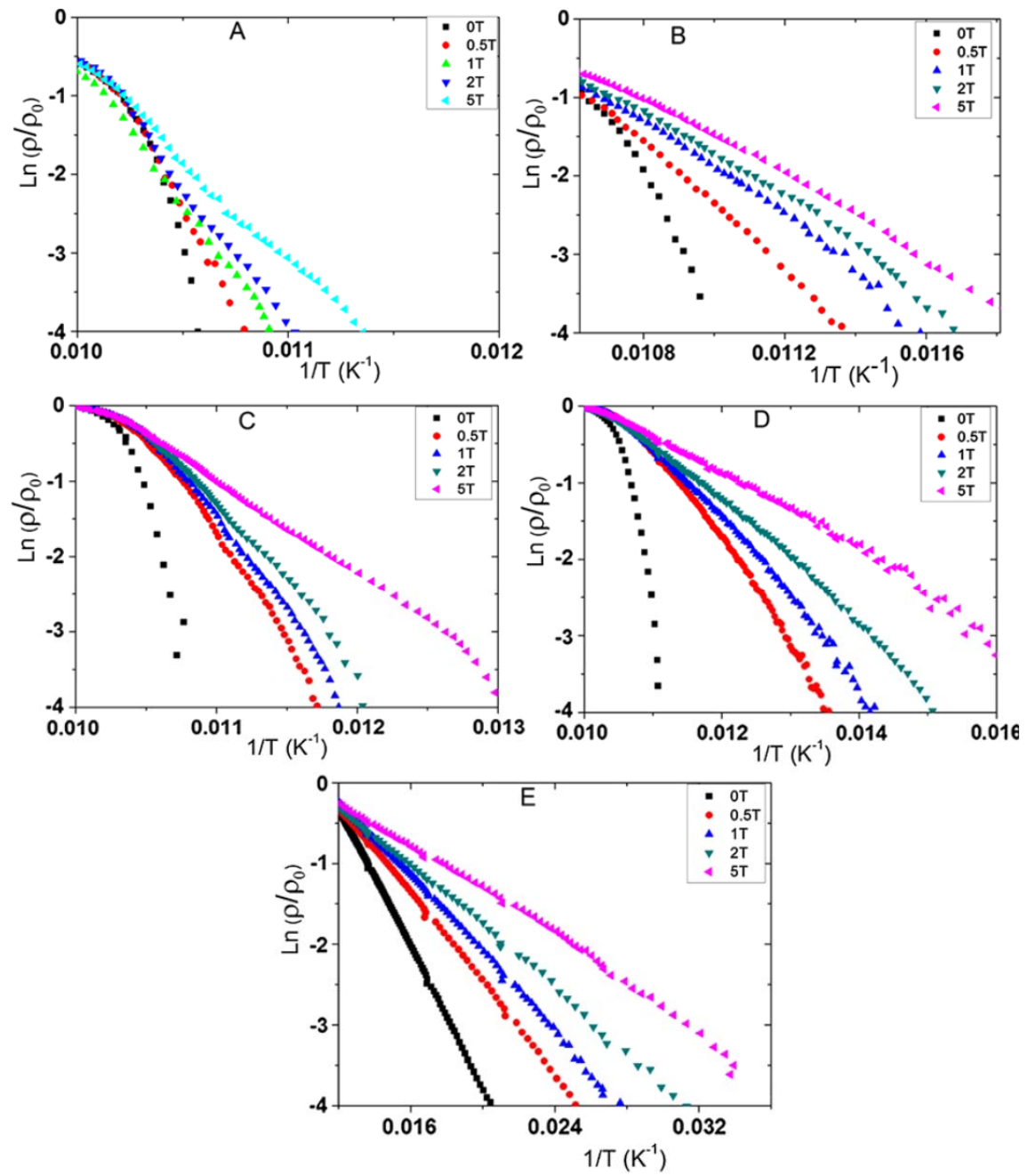


Figure 7

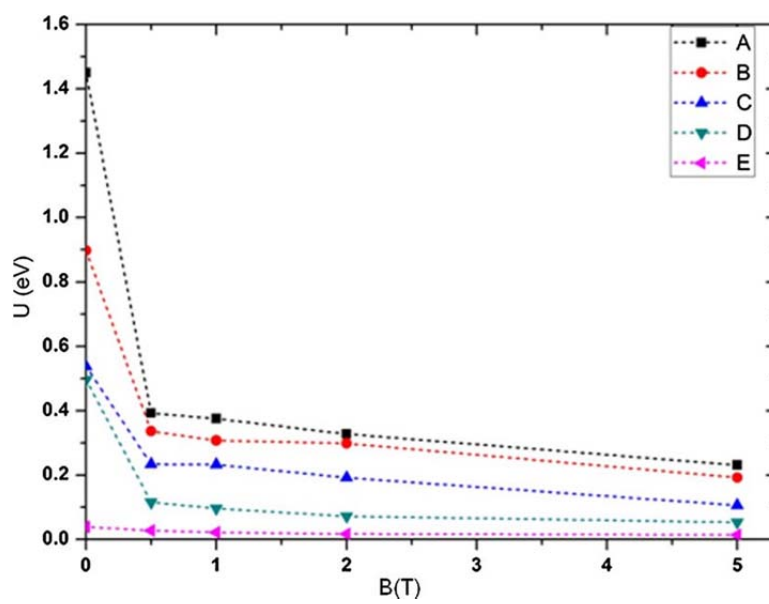


Figure 8